

Measurement of the branching fraction for the decay $B_s^0 \rightarrow D_s K \pi \pi$, relative to the $B_s^0 \rightarrow D_s \pi \pi \pi$ decay

P. d'Argent¹, E. Gersabeck¹, M. Kecke¹, M. Schiller²

¹*Physikalisches Institut, Ruprecht-Karls-Universität Heidelberg, Heidelberg, Germany*

²*European Organization for Nuclear Research (CERN), Geneva, Switzerland*

Abstract

We present the measurement of the branching fraction of decay $B_s^0 \rightarrow D_s K \pi \pi$ using the complete 3 fb^{-1} of data, collected during Run 1 of the LHC. The branching fraction is measured relative to the decay $B_s^0 \rightarrow D_s \pi \pi \pi$, from which we obtain

$$\frac{\mathcal{B}(B_s^0 \rightarrow D_s K \pi \pi)}{\mathcal{B}(B_s^0 \rightarrow D_s \pi \pi \pi)} = 0.051 \pm 0.002 \pm 0.003$$

The $B_s^0 \rightarrow D_s K \pi \pi$ decay can be further used to measure the weak CKM phase γ in a time-dependent analysis of the B_s^0 and \bar{B}_s^0 decay rates. This will be the final goal of the presented analysis.

Contents

| | | |
|----------|---|-----------|
| 1 | Introduction | 1 |
| 2 | Data samples | 1 |
| 3 | Selection | 2 |
| 3.1 | Cut-based selection | 2 |
| 3.2 | Multivariate stage | 4 |
| 4 | Simulated samples | 7 |
| 5 | Models for signal and background components in invariant mass spectrum | 10 |
| 5.1 | Signal models for $m(D_s\pi\pi\pi)$ and $m(D_sK\pi\pi)$ | 10 |
| 5.2 | Background models for $m(D_s\pi\pi\pi)$ | 10 |
| 5.3 | Background models for $m(D_sK\pi\pi)$ | 11 |
| 6 | Mass fits for signal and normalization | 13 |
| 6.1 | Fit to $B_s^0 \rightarrow D_s\pi\pi\pi$ candidates | 13 |
| 6.2 | Fit to $B_s^0 \rightarrow D_sK\pi\pi$ candidates | 13 |
| 7 | Efficiency corrections | 13 |
| 7.1 | Relative efficiency for BR measurement | 13 |
| 8 | Systematic errors | 16 |
| 9 | Results and summary | 19 |
| A | Appendix | 21 |
| A.1 | High Level Trigger requirements | 21 |
| A.2 | Re-weghted MC observables | 21 |
| | References | 23 |

1 Introduction

The weak phase γ is the least well known angle of the CKM unitary triangle. A key channel to measure γ is the time-dependent analysis of $B_s^0 \rightarrow D_s K$ decays [1], [2]. The $B_s^0 \rightarrow D_s K \pi \pi$ proceeds at tree level via the transitions shown in Fig. 1.1 a) and b).

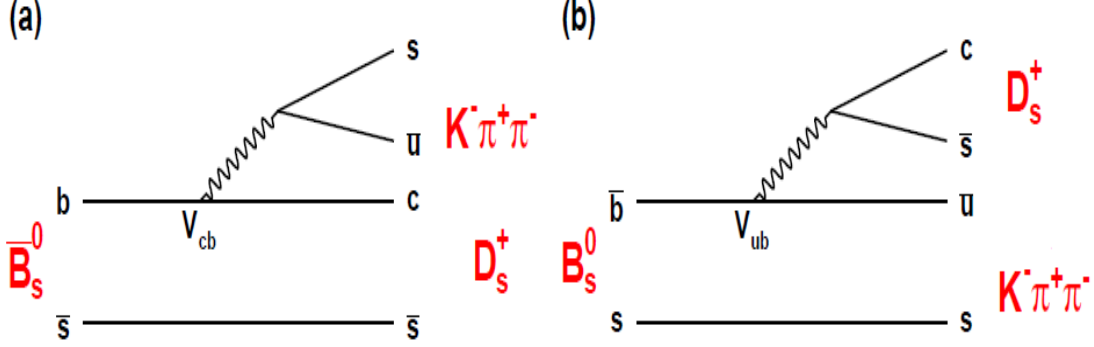


Figure 1.1: Feynman diagram of the $B_s^0 \rightarrow D_s K \pi \pi$ decay, proceeding via a) $b \rightarrow c$ transitions or b) $b \rightarrow u$ transitions.

To measure the weak CKM phase $\gamma \equiv \arg[-(V_{ud}V_{ub}^*)/(V_{cd}V_{cb}^*)]$, a decay with interference between $b \rightarrow c$ and $b \rightarrow u$ transitions at tree level is needed [1]. As illustrated in Fig. 1.1, this is the case for the presented decay mode. A measurement of γ using $B_s^0 \rightarrow D_s K \pi \pi$ decays, where the $K \pi \pi$ subsystem is dominated by excited kaon states such as the $K_1(1270)$ and $K_1(1400)$ resonances, will succeed the branching ratio measurement presented in this note. It is complementary to the above mentioned analysis of $B_s^0 \rightarrow D_s K$, making use of a fully charged final state, where every track is detected in the vertex locator. To account for the non-constant strong phase across the Dalitz plot, one can either develop a time-dependent amplitude model or select a suitable phase-space region and introduce a coherence factor as additional hadronic parameter to the fit.

This analysis is based on the first observation of the $B_s^0 \rightarrow D_s K \pi \pi$ decay presented in [3] and [4], where its branching ratio is measured relative to $B_s^0 \rightarrow D_s \pi \pi \pi$. The result obtained by the previous analysis is $0.052 \pm 0.005 \pm 0.003$, where the uncertainties are statistical and systematical, respectively. The branching ratio measurement is updated, exploiting the full Run 1 data sample, corresponding to 3 fb^{-1} of integrated luminosity.

2 Data samples

We use the full Run 1 sample from Stripping 21 with Reco14, consisting of 3 fb^{-1} of data, collected in the years 2011 and 2012 at a center of mass energies of 7 TeV and 8 TeV, respectively. The selected B_s^0 -candidates are required to pass the L0 Hadron trigger on

24 signal (TOS) or the L0 Global trigger independent of signal (TIS).
 25 Events that pass the L0 stage are further required to pass the HLT1 TrackAllL0 trigger
 26 on signal (TOS).
 27 All remaining candidates have to pass either the 2, 3 or 4-body topological trigger (TOS)
 28 of the HLT2 stage. More information on the HLT lines used in this analysis is given in
 29 Appendix A.1.
 30 For the presented analysis the B02DKPiPiD2HHHPIDBeauty2CharmLine is used to pres-
 31 elect signal $B_s^0 \rightarrow D_s K \pi \pi$ candidates and the B02DPiPiPiD2HHHPIDBeauty2CharmLine
 32 is used for the selection of $B_s^0 \rightarrow D_s \pi \pi \pi$ candidates. Both stripping lines employ the same
 33 selection cuts for the B_s^0 , D_s , K and π candidates. A summary of those cuts can be found in
 34 Table 2.1. In this table and throughout the note, we abbreviate $B_s^0 \rightarrow D_s X_s (\rightarrow K \pi \pi)$ and
 35 $B_s^0 \rightarrow D_s X_d (\rightarrow \pi \pi \pi)$, identifying $X_s \rightarrow K \pi \pi$ and $X_d \rightarrow \pi \pi \pi$ as the various resonances
 36 through which the decays proceed. The following text describes variables that might be
 37 ambiguous and/or cuts which benefits are not straight forward.
 38 In Table 2.1, DOCA is the abbreviation for distance of closest approach. This variable is
 39 used to ensure that all D_s and $X_{s,d}$ daughters originate from the same vertex. The minimal
 40 flight distance (FD) χ^2 is a measure on how likely a particle traveled some distance before
 41 it decayed. A cut on this variable is employed to reject prompt background for D_s and $X_{s,d}$
 42 candidates. DIRA is the abbreviation for the cosine of the angle θ between the hadron's
 43 flight direction \vec{x} and it's corresponding momentum vector \vec{p} , $\cos \theta_{\vec{x}-\vec{p}}$. For signal hadrons
 44 this variable is expected to be very close to one, while it can be arbitrary distributed for
 45 background.

46 **3 Selection**

47 A two-fold approach is used to isolate the $B_s^0 \rightarrow D_s K \pi \pi$ candidates from data passing
 48 the stripping line. First, further one-dimensional cuts are applied to reduce the level of
 49 combinatorial background and to veto some specific physical background. After that, a
 50 multivariate classifier is trained which combines the information of several input vari-
 51 ables, including their correlation, into one powerful discriminator between signal and
 52 combinatorial background.

53 **3.1 Cut-based selection**

54 In order to minimize the contribution of combinatorial background to our samples, we
 55 apply the following cuts to the b hadron:

- 56 (i) $\text{DIRA} > 0.99994$
- 57 (ii) $\min \text{IP } \chi^2 < 20$ to any PV
- 58 (iii) $\text{FD } \chi^2 > 100$ to any PV
- 59 (iv) $\text{Vertex } \chi^2/\text{nDoF} < 8$

| Variable | Stripping Cut |
|--|---|
| Track χ^2/nDoF | < 3 |
| Track p | $> 1000 \text{ MeV}/c$ |
| Track p_T | $> 100 \text{ MeV}/c$ |
| Track IP χ^2 | > 4 |
| D_s Daughter p_T | $\Sigma_{i=1}^3 p_i > 1800 \text{ MeV}/c$ |
| D_s Daughter DOCA | $< 0.5 \text{ mm}$ |
| D_s mass m_{D_s} | within $\pm 40 \text{ MeV}/c^2$ of PDG value |
| D_s Vertex χ^2/nDoF | < 10 |
| D_s min FD χ^2 | > 36 |
| X_d Daughter p_T | $> 2 \text{ GeV}/c$ |
| $X_{s,d}$ Daughter DOCA | $< 0.4 \text{ mm}$ |
| $X_{s,d}$ Daughter p_T | $\Sigma_{i=1}^3 p_{t,i} > 1250 \text{ MeV}/c$ |
| $X_{s,d}$ Vertex χ^2/nDoF | < 8 |
| $X_{s,d}$ min FD χ^2/nDoF | > 16 |
| $X_{s,d}$ DIRA | > 0.98 |
| $X_{s,d}$ $\Delta\rho$ (vertex displacement perpendicular to z-axis) | $> 0.1 \text{ mm}$ |
| $X_{s,d}$ ΔZ (vertex displacement along z-axis) | $> 2.0 \text{ mm}$ |
| B_s^0 DIRA | > 0.98 |
| B_s^0 min IP χ^2 | < 25 |
| B_s^0 Vertex χ^2/nDoF | < 10 |
| B_s^0 $\tau_{B_s^0}$ | $> 0.2 \text{ ps}$ |
| K DLL $_{K\pi}$ | > -5 |
| π DLL $_{K\pi}$ | < 10 |

Table 2.1: Summary of the stripping selections for $B_s^0 \rightarrow D_s K \pi \pi$ decays.

(v) $(Z_{D_s} - Z_{B_s^0}) > 0$, where Z_M is the z-component of the position \vec{x} of the decay vertex for the B_s^0/D_s meson

Additionally, we veto various physical backgrounds, which have either the same final state as our signal decay, or can contribute via a single misidentification of $K \rightarrow \pi$ or $K \rightarrow p$:

- $B_s^0 \rightarrow D_s^+ D_s^- : |M(K\pi\pi) - m_{D_s}| > 20 \text{ MeV}/c^2$
- $B_s^0 \rightarrow D_s^- K^+ K^- \pi^+ : \text{possible with single missID of } K^- \rightarrow \pi^-, \text{ rejected by requiring } \pi^- \text{ to fulfill } \text{DLL}_{K\pi} < 5$
- $B^0 \rightarrow D^+(\rightarrow K^+ \pi^- \pi^+) K \pi \pi : \text{possible with single missID of } \pi^+ \rightarrow K^+, \text{ vetoed by changing particle hypothesis and recompute } |M(K^+ \pi^- \pi^+) - m_{D_p}| > 20 \text{ MeV}/c^2, \text{ or the } K^+ \text{ has to fulfill } \text{DLL}_{K\pi} > 10$

- $\Lambda_b^0 \rightarrow \Lambda_c^+(\rightarrow pK^-\pi^+)K\pi\pi$: possible with single missID of $p \rightarrow K^+$, vetoed by changing particle hypothesis and recompute $M(pK^-\pi^+) - m_{\Lambda_c^+} > 15 \text{ MeV}/c^2$, or the K^+ has to fulfill $(\text{DLL}_{K\pi} - \text{DLL}_{p\pi}) > 0$

All signal candidates used in the branching ratio measurement are reconstructed via the $D_s \rightarrow K^+K^-\pi^+$ channel. This decay can either proceed via the narrow ϕ resonance, the broader K^{*0} resonance, or non resonant. Depending on the decay process being resonant or not, we apply additional PID requirements:

1. resonant case:

- (a) $D_s^+ \rightarrow \phi\pi^+$, with $|M(K^+K^-) - m_\phi| < 20 \text{ MeV}/c^2$: no additional requirements, since ϕ is narrow and almost pure K^+K^- .
- (b) $D_s^+ \rightarrow \bar{K}^{*0}K^+$, with $|M(K^-\pi^+) - m_{K^{*0}}| < 75 \text{ MeV}/c^2$: $\text{DLL}_{K\pi} > 0$ for kaons, since this resonance is more than ten times broader than ϕ .

2. non resonant case: $\text{DLL}_{K\pi} > 5$ for kaons, since the non resonant category has significant charmless contributions.

Since a measurement of the weak CKM phase γ in the $B_s^0 \rightarrow D_s K\pi\pi$ channel will almost certainly be statistically limited, we plan to add also the $D_s \rightarrow \pi\pi\pi$ final state with $\mathcal{BR}(D_s \rightarrow \pi\pi\pi) \approx 0.2 \cdot \mathcal{BR}(D_s \rightarrow KK\pi)$ to the γ analysis. Since the determination of the branching ratio is expected to have the same level of statistical and systematical uncertainties and due to the additional complexity (different selection, efficiencies, simulated samples), we choose to only use the most prominent $D_s \rightarrow KK\pi$ final state for the BR determination.

3.2 Multivariate stage

We use TMVA [5] to train a multivariate discriminator, which is used to further improve the signal to background ratio. The 17 variables used for the training are:

- $\max(\text{ghostProb})$ over all tracks
- $\text{cone}(p_T)$ asymmetry of every track, which is defined to be the difference between the p_T of the π/K and the sum of all other p_T in a cone of radius $r = \sqrt{(\Delta\Phi)^2 + (\Delta\eta)^2} < 1$ rad around the signal π/K track.
- $\min(\text{IP}\chi^2)$ over the X_s daughters
- $\max(\text{DOCA})$ over all pairs of X_s daughters
- $\min(\text{IP}\chi^2)$ over the D_s daughters
- D_s and B_s^0 DIRA

- D_s FD significance
- $\max(\cos(D_s h_i))$, where $\cos(D_s h_i)$ is the cosine of the angle between the D_s and another track i in the plane transverse to the beam
- B_s^0 IP χ^2 , FD χ^2 and Vertex χ^2

Various classifiers were investigated in order to select the best performing discriminator. Consequently, a boosted decision tree with gradient boost (BDTG) is chosen as nominal classifier. We use truth-matched MC as signal input. Simulated signal candidates are required to pass the same trigger, stripping and preselection requirements, that were used to select the data samples. For the background we use events from the high mass sideband ($m_{B_s^0 \text{ candidate}} > 5600 \text{ MeV}/c^2$) of our data samples. As shown in Fig. 3.1, this mass region is sufficiently far away from signal structures and is expected to be dominantly composed of combinatorial background.

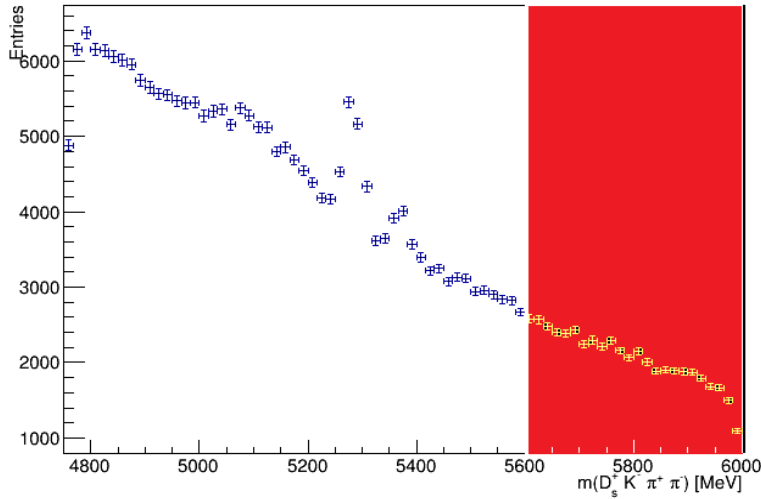


Figure 3.1: Invariant mass distribution of preselected $B_s^0 \rightarrow D_s K \pi \pi$ candidates. The red coloured region with $m_{B_s^0 \text{ candidate}} > 5600 \text{ MeV}/c^2$ is used as background input for the boosted decision tree.

The distributions of the input variables for signal and background are shown in Fig. 3.2.

The relative importance of the input variables for the BDTG training is summarized in Table 3.1.

The BDTG output distribution for test and training samples is shown in Fig 3.3. No sign of overtraining is observed.

We determine the optimal cut value by maximizing the figure of merit $S/\sqrt{S+B}$ where S is the signal yield and B the background yield in the signal region, defined to be

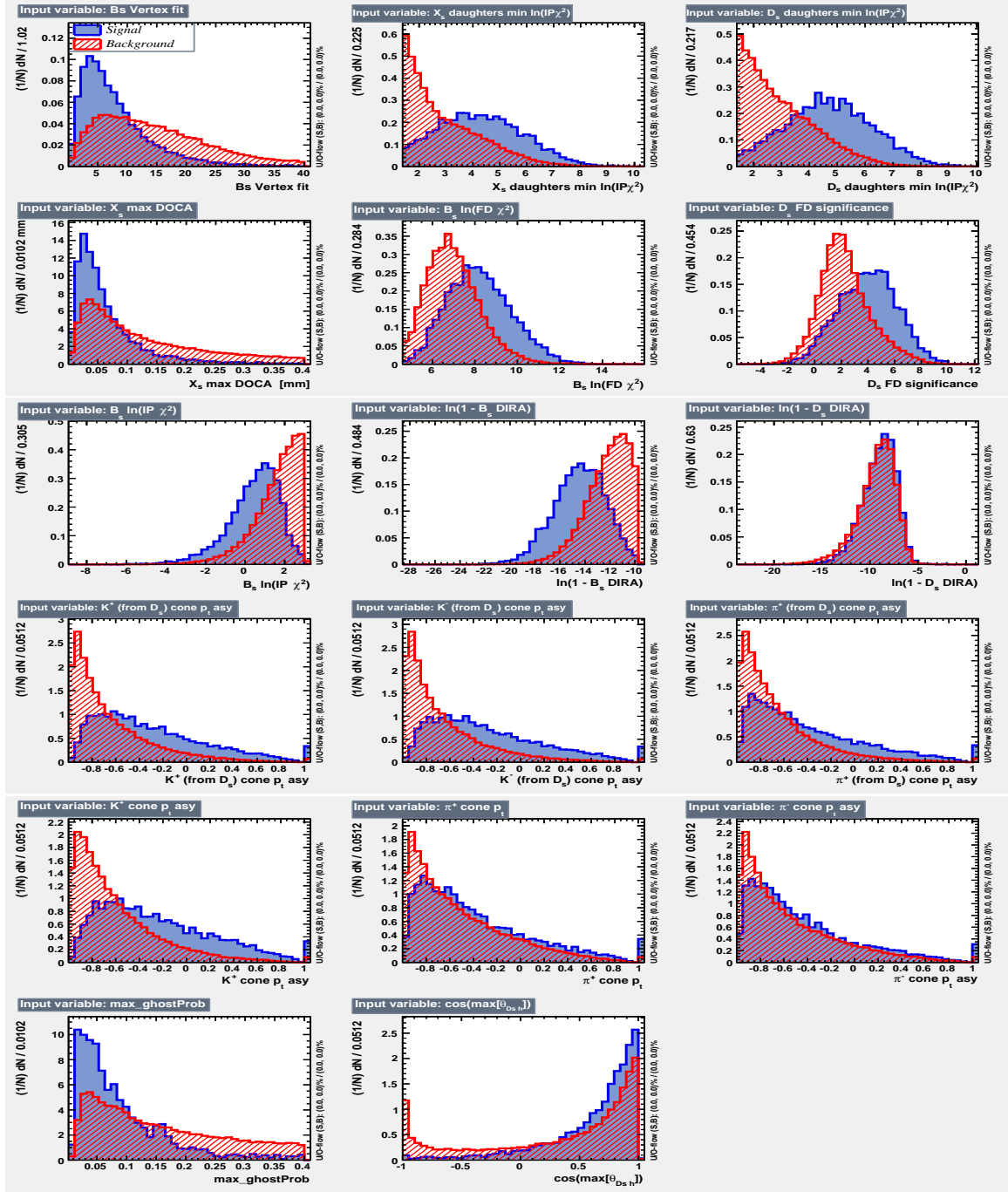


Figure 3.2: Distributions of the input variables used in the BDTG training. The background is shown as red hatched, while the signal is depicted solid blue.

124 within ± 50 MeV/ c^2 of the nominal B_s^0 mass. To avoid a bias in the determination of the
 125 branching fraction, we determine S and B using our normalization channel. All trigger,
 126 stripping and additional selection criteria described in this and the previous chapter are

| Variable | relative importance [%] |
|----------------------------|-------------------------|
| pi_minus_ptasy_1.00 | 7.32 |
| log_Ds_FDCHI2_ORIVX | 7.23 |
| K_plus_ptasy_1.00 | 7.17 |
| log_Ds_DIRA | 6.96 |
| Bs_ENDVERTEX_CHI2 | 6.82 |
| max_ghostProb | 6.76 |
| pi_plus_ptasy_1.00 | 6.57 |
| log_DsDaughters_min_IPCHI2 | 6.21 |
| log_Bs_DIRA | 6.15 |
| K_plus_fromDs_ptasy_1.00 | 6.10 |
| log_XsDaughters_min_IPCHI2 | 5.87 |
| K_minus_fromDs_ptasy_1.00 | 5.62 |
| cos(Ds h) | 5.58 |
| log_Bs_IPCHI2_OWNPV | 5.08 |
| log_Bs_FDCHI2_OWNPV | 4.04 |
| Xs_max_DOCA | 3.98 |
| pi_minus_fromDs_ptasy_1.00 | 2.59 |

Table 3.1: Summary of the relative importance of each variable in the training of the BDTG.

127 applied to the $B_s^0 \rightarrow D_s \pi \pi \pi$ data samples. After that, we perform a simplified version of
 128 the fit to the invariant mass distribution of $B_s^0 \rightarrow D_s \pi \pi \pi$ candidates described in Sec. 6.
 129 Here, a Gaussian function to model the signal and an exponential function to model
 130 combinatorial background is used. From this fit we estimate the number of signal events
 131 in our normalization channel. Multiplying that number with the PDG branching fraction
 132 of $\frac{\mathcal{B}(B_s^0 \rightarrow D_s K \pi \pi)}{\mathcal{B}(B_s^0 \rightarrow D_s \pi \pi \pi)}$ and the ratio of efficiencies discussed in Sec. 7 allows us to estimate the
 133 expected number of $B_s^0 \rightarrow D_s K \pi \pi$ signal decays. The number of background events can
 134 then be computed as

$$N_{bkg} = N_{all} - N_{sig}|_{m_{B_s^0} \pm 50 \text{ MeV}/c^2}. \quad (3.1)$$

135 The efficiency curves as a function of the cut value are shown in Fig. 3.4. The optimal
 136 cut value is found to be $\text{BDTG} > 0.7012$. At this working point the signal efficiency is
 137 estimated to be 72.47 %, while the background rejection in the signal region is 97.38 %.

138 4 Simulated samples

139 The simulated (MC) samples are generated using Pythia 8 with Sim08 and Gauss v45r11.
 140 Samples are reconstructed with Brunel v43r2p11 and the DSTs were processed using
 141 DaVinci v36r1p1. The event numbers for the simulated $B_s^0 \rightarrow D_s K \pi \pi$ and $B_s^0 \rightarrow D_s \pi \pi \pi$
 142 samples, as well as the amount of generated and selected events, is shown in Tab. 4.1 and

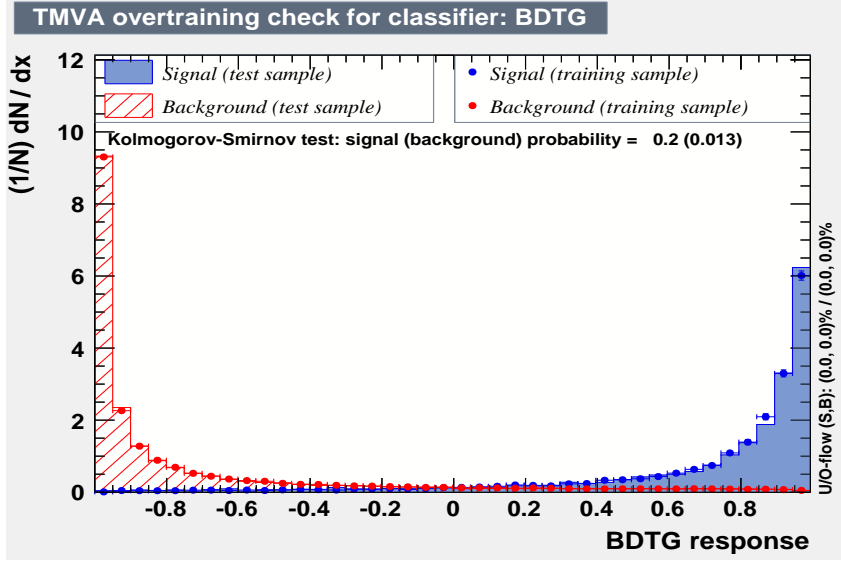


Figure 3.3: BDTG output classifier distribution for (blue) signal and (red) background. The response of an independent test sample (dots) is overlaid.

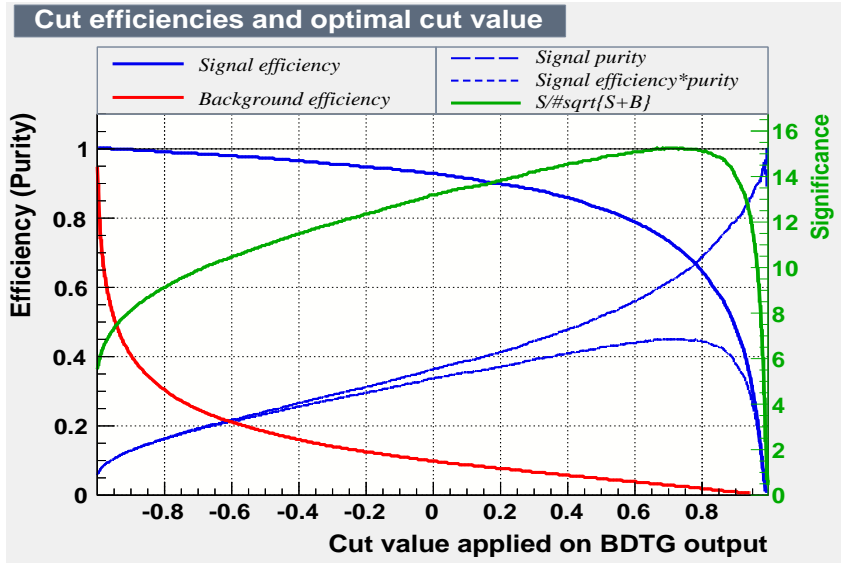


Figure 3.4: Efficiency and purity curves for (blue) signal, (red) background and the (green) FoM curve, as a function of the chosen cut value.

143 4.2 for the different center of mass energies.

144 In order to use our MC samples during the BDT training, described in Chapter 3, and the
 145 calculation of efficiencies (Chapter 7), we have to ensure that the $B_s^0 \rightarrow D_s K \pi \pi$ decay is
 146 modeled correctly by the simulation. To check this, we compare distributions of observables
 147 which we use during the multivariate selection stage, as well as some key event observables.
 148 The compared distributions need to be generated by signal decays only, therefore we

| Quantity | $B_s^0 \rightarrow D_s K \pi \pi$ | $B_s^0 \rightarrow D_s \pi \pi \pi$ |
|------------------|-----------------------------------|-------------------------------------|
| event type | 1326607 | 1326606 |
| events generated | 1,131,662 | 1,188,549 |
| events selected | 14,480 | 15,793 |

Table 4.1: Generated and selected MC events for signal and normalization channel at $\sqrt{s} = 7 \text{ TeV}$.

| Quantity | $B_s^0 \rightarrow D_s K \pi \pi$ | $B_s^0 \rightarrow D_s \pi \pi \pi$ |
|------------------|-----------------------------------|-------------------------------------|
| event type | 1326607 | 1326606 |
| events generated | 1,257,244 | 1,167,428 |
| events selected | 14,422 | 13,423 |

Table 4.2: Generated and selected MC events for signal and normalization channel at $\sqrt{s} = 8 \text{ TeV}$.

149 truth-match all particles in the MC samples. Signal distributions of observables in data
150 are obtained using the sWeight technique [6]. Due to the lack of a clear signal peak in
151 the $B_s^0 \rightarrow D_s K \pi \pi$ data after the stripping, trigger and cut-based preselection, we use
152 preselected $B_s^0 \rightarrow D_s \pi \pi \pi$ candidates to obtain signal sWeights: We perform a fit of a
153 Gaussian signal model and an exponential background to the invariant mass distribution
154 of $B_s^0 \rightarrow D_s \pi \pi \pi$ candidates. Using the weights generated from this fit, we weight the
155 distributions of data observables in $B_s^0 \rightarrow D_s K \pi \pi$ and obtain the corresponding signal
156 distributions.
157 Figure 4.1 shows the distribution of the number of tracks per event and the distribution of
158 the maximum ghost probability over all tracks in MC and data.

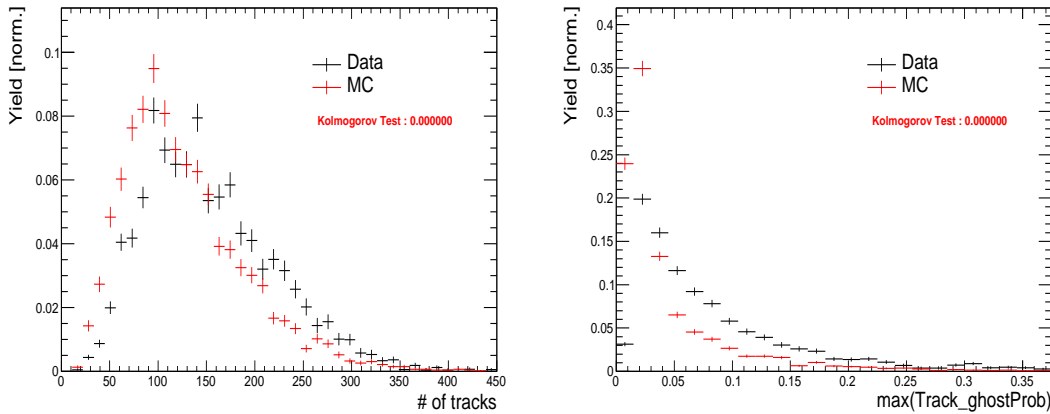


Figure 4.1: Comparison between the distribution of (left) the number of tracks and (right) the maximum ghost probability over all tracks in (black) data and (red) simulation.

159 In both cases, the distributions differ significantly. Therefore, we reweight the MC
160 samples using those two variables. The reweighting is done successively, e.g. we perform

two 1D weighting processes, where we equalize the respective MC distribution to the observed distribution in data. All distributions of observables used in the BDT training, before and after the reweighting procedure, are shown in the Appendix A.2.

5 Models for signal and background components in invariant mass spectrum

The expected signal shape, as well as the expected shape for the combinatorial and physical background has to be known in order to properly model the invariant mass distribution of $B_s^0 \rightarrow D_s K \pi \pi$ and $B_s^0 \rightarrow D_s \pi \pi \pi$ candidates.

5.1 Signal models for $m(D_s \pi \pi \pi)$ and $m(D_s K \pi \pi)$

The mass distribution of $B_s^0 \rightarrow D_s K \pi \pi$ signals is modeled using two Gaussian functions, which share the same mean μ , but are allowed to have different widths σ_1 and σ_2 . Another double Gaussian function is used to account for the contribution of the $B^0 \rightarrow D_s K \pi \pi$ decay, which is also present in the $m(D_s K \pi \pi)$ spectrum. All parameters of both double Gaussians, except the core width σ_1 , are allowed to float in the fit. The core width is fixed to the value obtained from simulation in order to improve the stability of the fit.

The same approach is used to describe the invariant mass distribution of $B_s^0 \rightarrow D_s \pi \pi \pi$ candidates. A double Gaussian function is used to model the signal, all parameters except the core width σ_1 are allowed to float.

5.2 Background models for $m(D_s \pi \pi \pi)$

Different background sources arise in the invariant mass spectrum of candidates in the normalization mode.

The following backgrounds have to be accounted for:

- Combinatorial background: This contribution arises from either a real D_s , which is paired with random tracks to form the B_s^0 candidates, or via real X_d 's, which are combined with three tracks that fake a D_s candidate to form a fake B_s^0 .
- Partially reconstructed $B_s^0 \rightarrow D_s^* \pi \pi \pi$ decays, with $D_s^* \rightarrow D_s \gamma$ or $D_s^* \rightarrow D_s \pi^0$, where the γ/π^0 is not reconstructed in the decay chain.

In both cases of combinatorial background, the distribution in the invariant mass of B_s^0 candidates is expected to be smooth and decrease with higher masses. Therefore, one exponential function is used to model these contributions.

The shape of the $B_s^0 \rightarrow D_s^* \pi \pi \pi$ contribution is expected to be peaking in the $m(D_s \pi \pi \pi)$ spectrum, with large tails due to the missing momentum, which is carried away by the π^0 or γ . We rely on simulation to estimate the shape of this contribution.

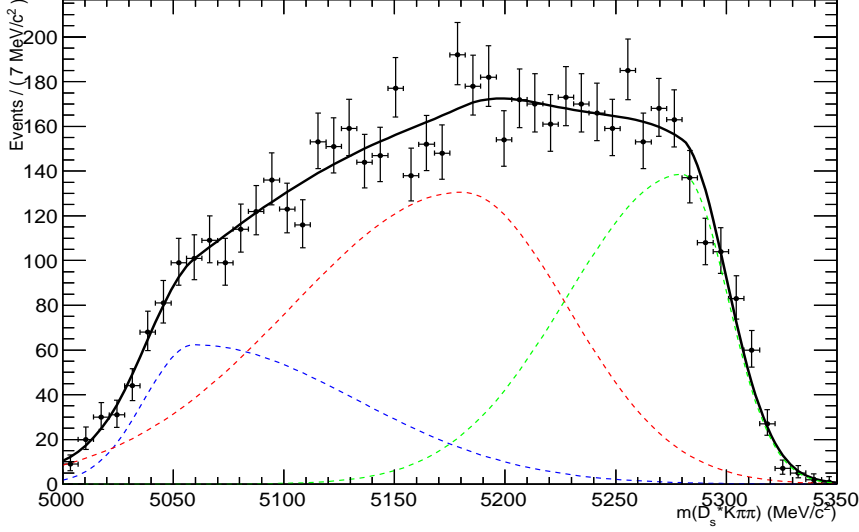


Figure 5.1: Invariant mass distribution of simulated $B_s^0 \rightarrow D_s^* \pi \pi \pi$ events, where the γ/π^0 is excluded from the reconstruction. A fit of the sum of three bifurcated Gaussian functions to this distribution is overlaid.

Figure 5.1 shows the fit of the sum of three bifurcated Gaussian functions to the invariant mass distribution of simulated $B_s^0 \rightarrow D_s^* \pi \pi \pi$ event. The pion or photon from $D_s^* \rightarrow D_s(\gamma/\pi^0)$ is excluded from the reconstruction. The obtained shape parameters are used as input values for the nominal $m(D_s \pi \pi \pi)$ mass fit. The yield of this contribution is directly determined in the nominal fit.

5.3 Background models for $m(D_s K \pi \pi)$

For the signal channel, the following background sources have to be considered:

- Combinatorial background: same contributions as discussed in Sec. 5.2.
- Partially reconstructed $B_s^0 \rightarrow D_s^* K \pi \pi$ decays, with $D_s^* \rightarrow D_s \gamma$ or $D_s^* \rightarrow D_s \pi^0$, where the γ/π^0 is not reconstructed in the decay chain.
- Partially reconstructed $B^0 \rightarrow D_s^* K \pi \pi$ decays, with $D_s^* \rightarrow D_s \gamma$ or $D_s^* \rightarrow D_s \pi^0$, where the γ/π^0 is not reconstructed in the decay chain.
- Misidentified $B_s^0 \rightarrow D_s \pi \pi \pi$ decays, where one of the pions is wrongly identified as a kaon $\pi \rightarrow K$.
- Misidentified, partially reconstructed $B_s^0 \rightarrow D_s^* \pi \pi \pi$ decays, where one of the pions is wrongly identified as a kaon $\pi \rightarrow K$ and the γ/π^0 from $D_s^* \rightarrow D_s \gamma/\pi^0$ is not reconstructed.

211 The combinatorial background is expected to be flat in the spectrum of the invariant
 212 mass of $B_s^0 \rightarrow D_s K \pi \pi$ candidates. An exponential function is used to model this contri-
 213 bution.
 214 The shape of the partially reconstructed background without misID is taken from our
 215 normalization channel, where it can be directly fitted by the sum of three bifurcated
 216 Gaussian functions as described above. In the signal mass fit, all shape parameters for the
 217 $B_s^0 \rightarrow D_s^* K \pi \pi$ background are fixed to the input values from our normalization fit.
 218 For the contribution of the $B^0 \rightarrow D_s^* K \pi \pi$ background, the same shape is used but
 219 the means μ_i of the bifurcated gaussians are shifted down by $m_{B_s^0} - m_{B^0}$ [7]. The yields
 220 of both contributions are directly determined in the nominal fit.
 221 To determine the shape of misidentified $B_s^0 \rightarrow D_s \pi \pi \pi$ candidates in the $m(D_s K \pi \pi)$
 222 spectrum, we take a truth-matched signal MC sample of our normalization channel. We
 223 then use the PIDCalib package to determine the $\pi \rightarrow K$ fake rate. For every candidate
 224 in our MC sample, a (momentum) p_{tot} and (pseudorapidity) η -dependent event weight
 225 is computed and assigned. We flip the particle hypothesis from pion to kaon for the π
 226 with the biggest miss-ID weight for each event and recompute the invariant B_s^0 mass. This
 227 distribution is then modeled using two Crystal Ball functions. The distribution and the fit
 228 are shown in Fig. 5.2(left).

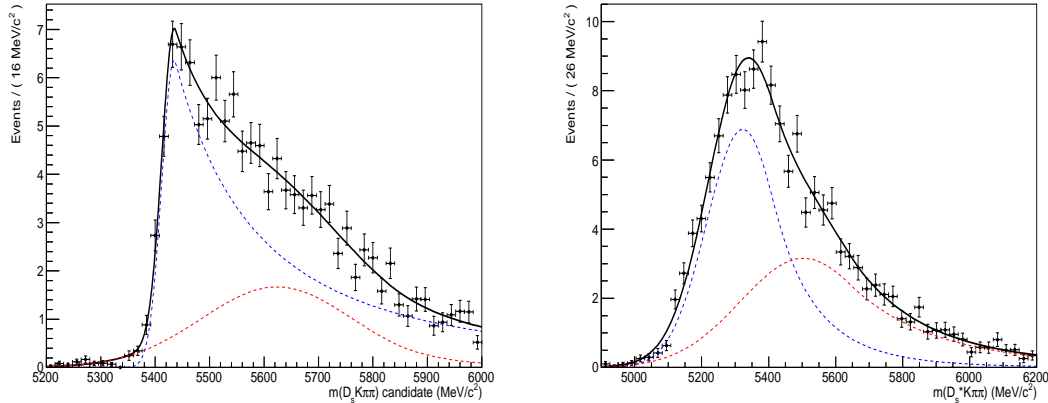


Figure 5.2: Invariant mass distribution of (left) simulated $B_s^0 \rightarrow D_s \pi \pi \pi$ events, where one of the π 's is reconstructed as a K and the misID probability for each event is taken into account. The corresponding distribution for simulated $B_s^0 \rightarrow D_s^* \pi \pi \pi$ events, where the γ/π^0 from the D_s^* is excluded from reconstruction, is shown on the right. The solid, black curve on each plot corresponds to the fit consisting of two Crystal Ball functions.

229 The expected yield of misidentified $B_s^0 \rightarrow D_s \pi \pi \pi$ candidates in the $m(D_s K \pi \pi)$ spec-
 230 trum is computed by multiplying the fake probability of $\propto 3.2\%$, which is derived from
 231 PIDCalib, by the yield of $B_s^0 \rightarrow D_s \pi \pi \pi$ signal candidates, determined in the nominal mass
 232 fit of our normalization channel.
 233 In the same way as mentioned above, we can determine the rate of misidentified, partially
 234 reconstructed $B_s^0 \rightarrow D_s^* \pi \pi \pi$ decays in our sample of $B_s^0 \rightarrow D_s K \pi \pi$ decays using PIDCalib

and a MC sample of $B_s^0 \rightarrow D_s^* \pi \pi \pi$ events. The invariant mass distribution we obtain when we exclude the γ/π^0 , flip the the particle hypothesis $\pi \rightarrow K$ and apply the event weights given by the fake rate, is shown in Fig. 5.2 (right). The fit of two Crystal Ball functions to this distribution is overlaid. The yield of this contribution is determined from the yield of $B_s^0 \rightarrow D_s^* \pi \pi \pi$ candidates in the nominal mass fit of our normalization channel, multiplied by the misID probability of $\propto 3.6\%$.

6 Mass fits for signal and normalization

This section describes the fits to the invariant mass distribution of $B_s^0 \rightarrow D_s K \pi \pi$ and $B_s^0 \rightarrow D_s \pi \pi \pi$ candidates after all selections are applied. The obtained yields are summarized in Tab. 6.1.

6.1 Fit to $B_s^0 \rightarrow D_s \pi \pi \pi$ candidates

An unbinned maximum likelihood fit is performed simultaneously to the invariant mass distribution of $B_s^0 \rightarrow D_s \pi \pi \pi$ candidates, for 7 and 8 TeV data. As discussed in Sec. 5.1, the fit is given as the sum of the double Gaussian signal model, the sum of three bifurcated Gaussian functions to model the partially reconstructed $B_s^0 \rightarrow D_s^* \pi \pi \pi$ background and an Exponential function to account for combinatorial background. The invariant mass distribution and the fit is shown in Fig. 6.1.

6.2 Fit to $B_s^0 \rightarrow D_s K \pi \pi$ candidates

The shape of the invariant mass distribution of $B_s^0 \rightarrow D_s K \pi \pi$ candidates is described by the sum of two double Gaussian functions for the B^0 and B_s^0 signal, two sums of three bifurcated Gaussians for the $B_s^0/B^0 \rightarrow D_s^* K \pi \pi$ partially reconstructed background contributions and two sums of double Crystal Ball functions for the single misID $B_s^0 \rightarrow D_s \pi \pi \pi$ and the partially reconstructed, misidentified $B_s^0 \rightarrow D_s^* \pi \pi \pi$ decays. A simultaneous unbinned maximum likelihood fit is performed and the result is shown in Fig. 6.2.

7 Efficiency corrections

Several relative efficiency corrections are needed to measure the branching fraction of the $B_s^0 \rightarrow D_s K \pi \pi$ decay with respect to $B_s^0 \rightarrow D_s \pi \pi \pi$. Precise knowledge of the efficiency related to the detector acceptance, PID requirements, used trigger lines and offline selections are crucial for both, the determination of γ and the branching ratio measurement.

7.1 Relative efficiency for BR measurement

For the branching ratio measurement, the relative efficiency is given by

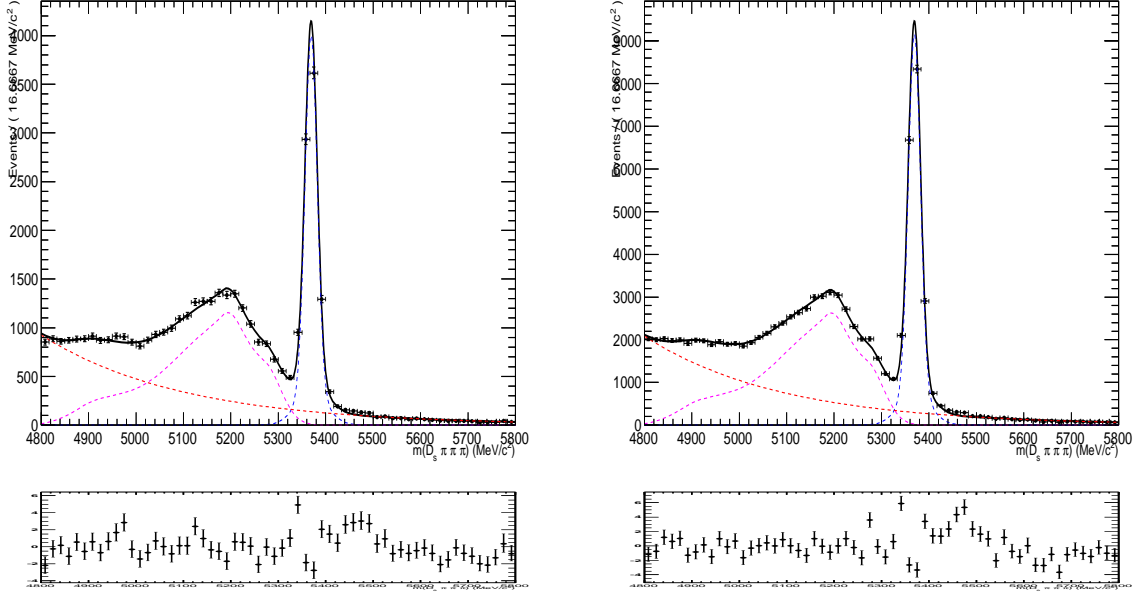


Figure 6.1: Invariant mass distribution of $B_s^0 \rightarrow D_s \pi \pi \pi$ candidates for (left) 2011 and (right) 2012 data. The fit described in the text is overlaid. The dashed lines show the (magenta) partially reconstructed and (red) combinatorial component, as well as the (blue) signal component. The pull distributions for the simultaneous fit are shown at the lower left and right.

| invariant mass spectrum/fit component | yield 2011 | yield 2012 |
|---------------------------------------|-----------------|-----------------|
| $m(D_s K \pi \pi)$ | | |
| $B_s^0 \rightarrow D_s K \pi \pi$ | 375 ± 26 | 866 ± 42 |
| $B^0 \rightarrow D_s K \pi \pi$ | 984 ± 44 | 2118 ± 72 |
| $B_s^0 \rightarrow D_s^* K \pi \pi$ | 765 ± 103 | 1705 ± 221 |
| $B^0 \rightarrow D_s^* K \pi \pi$ | 2048 ± 363 | 4564 ± 810 |
| $B_s^0 \rightarrow D_s \pi \pi \pi$ | 285 (fixed) | 650 (fixed) |
| $B_s^0 \rightarrow D_s^* \pi \pi \pi$ | 602 (fixed) | 1375 (fixed) |
| combinatorial | 5821 ± 145 | 12683 ± 216 |
| $m(D_s \pi \pi \pi)$ | | |
| $B_s^0 \rightarrow D_s \pi \pi \pi$ | 8496 ± 102 | 19410 ± 160 |
| $B_s^0 \rightarrow D_s^* \pi \pi \pi$ | 16730 ± 296 | 38180 ± 583 |
| combinatorial | 16640 ± 302 | 36606 ± 590 |

Table 6.1: Summary of yields from the fits to 2011 and 2012 data.

$$\epsilon_{rel} = \epsilon_{rel}^{acc} \cdot \epsilon_{rel}^{sel} \cdot \epsilon_{rel}^{pid}, \quad (7.1)$$

266 where $\epsilon = \frac{\epsilon_{Norm}}{\epsilon_{Sig}}$ is the ratio of the efficiency for the signal and normalization mode.

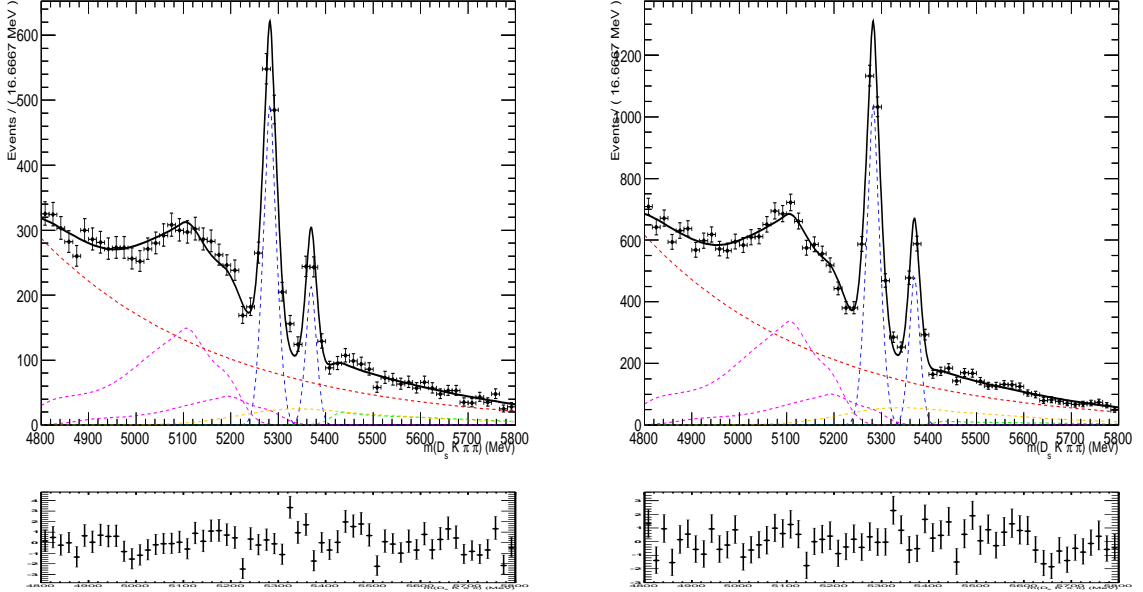


Figure 6.2: Invariant mass distribution of $B_s^0 \rightarrow D_s K \pi \pi$ candidates for (left) 2011 and (right) 2012 data. A fit described in the text is overlaid. The dashed lines show the (magenta) partially reconstructed and (red) combinatorial background, as well as the (blue) signal component. The dashed green line depicts the misID backgrounds and the dashed yellow line depicts the misidentified, partially reconstructed background component. The pull distributions for the simultaneous fit are shown at the lower left and right.

To evaluate these efficiencies, we rely on simulation. The three efficiencies given in Eq. 7.1 are:

- ϵ_{rel}^{acc} : This is the relative efficiency due to the geometrical acceptance of the LHCb detector. All tracks are required to have a polar angle between 10 and 400 mrad and a minimal momentum of $|p| > 1.6$ GeV/c in order to be recorded for further analysis. Since the particle species of one track differs between the signal and normalization mode, the efficiencies caused by the geometrical acceptance are expected to be slightly different for the two channels.
- ϵ_{rel}^{sel} : The relative selection efficiency due to trigger and offline requirements. This efficiency is evaluated using the simulated $B_s^0 \rightarrow D_s K \pi \pi$ and $B_s^0 \rightarrow D_s \pi \pi \pi$ samples, comparing the signal yield at generator level to the yield after the trigger and offline requirements are imposed. The respective yields used for the efficiency determination can be found in Tab. 4.1 and 4.2.
- ϵ_{rel}^{pid} : The relative PID efficiency due to the identification likelihood requirements for tracks from both modes. This is evaluated using efficiencies from $D^{*+} \rightarrow D^0(K^- \pi^+) \pi^+$ calibration data, which is weighted by the expected momentum (p)

283 distribution taken from simulation. The PIDCalib tool with a p - and η -dependent
 284 binning is used to perform this evaluation.

285 Using the definition given in Eq. 7.1, the branching ratio can be expressed as

$$\frac{\mathcal{B}(B_s^0 \rightarrow D_s K \pi \pi)}{\mathcal{B}(B_s^0 \rightarrow D_s \pi \pi \pi)} = \frac{\mathcal{Y}(B_s^0 \rightarrow D_s K \pi \pi)}{\mathcal{Y}(B_s^0 \rightarrow D_s \pi \pi \pi)} \cdot \epsilon_{rel}, \quad (7.2)$$

286 where $\mathcal{Y}(x)$ represents the yield of the respective channel.

287 The single efficiencies, as well as the total selection efficiency, for the signal and normaliza-
 288 tion channel, is given in Tab. 7.1.

| Efficiency (%) | $B_s^0 \rightarrow D_s K \pi \pi$ | $B_s^0 \rightarrow D_s \pi \pi \pi$ |
|-----------------------|-----------------------------------|-------------------------------------|
| 2011 ϵ^{acc} | 11.37 ± 0.02 | 10.66 ± 0.02 |
| 2012 ϵ^{acc} | 11.63 ± 0.02 | 10.90 ± 0.02 |
| 2011 ϵ^{sel} | 1.18 ± 0.01 | 1.21 ± 0.01 |
| 2012 ϵ^{sel} | 1.06 ± 0.01 | 1.05 ± 0.01 |
| 2011 ϵ^{pid} | 73.25 ± 0.88 | 88.50 ± 0.59 |
| 2012 ϵ^{pid} | 71.96 ± 0.90 | 88.39 ± 0.59 |
| 2011 total ϵ | 0.098 ± 0.002 | 0.114 ± 0.001 |
| 2012 total ϵ | 0.089 ± 0.001 | 0.101 ± 0.001 |

Table 7.1: Efficiencies due to the detector acceptance, selection requirements and PID cuts for the signal and normalization mode. All values are obtained using simulated events.

289 8 Systematic errors

290 Several systematic errors contribute to the overall uncertainty on the branching fractions.
 291 We consider the most significant ones:

- 292 • Particle identification
- 293 • Signal and background models
- 294 • Determination of the selection efficiency with MC
- 295 • The relative trigger efficiency
- 296 • The relative tracking efficiency
- 297 • MC statistics
- 298 • BDTG efficiency

| | baseline | alternative 1 | alternative 2 |
|------------------------|--|--|--|
| p bins [MeV/c] | 3000-9300-15600-19000 -24400-29800-35200-40600 -46000-51400-56800-62200 -67600-73000-78400-83800 -89200-94600-100000 | 0-10000-20000-30000-40000 -50000-60000-70000-80000-90000 -100000 | 1000-8450-15900-23350 -30800-38250-45700-53150 -60600-68050-75500-82950 -90400-97850-105300-112750 -120200-127650-135100-142550 -150000 |
| η bins | 1.5-2.375-3.25-4.125-5 | 2-2.3-2.6-2.9-3.2-3.5-3.8-4.1-4.4-4.7-5 | 1.5-2.2-3.1-4-5 |
| $\Delta\epsilon^{pid}$ | - | 0.4 % | 0.15 % |

Table 8.1: Summary of considered binning schemes for the determination of the PID efficiency using PIDCalib.

The particle identification (PID) efficiency is determined using PIDcalib in bins of pseudorapidity η and transverse momentum p_T of each B_s^0 candidate. To estimate the systematic uncertainty, the baseline binning scheme was changed to alternative η and p_T bins. Tab. 8.1 summarizes the tested binning schemes and the observed effect on ϵ^{pid} .

The maximum change in the PID efficiency due to the binning scheme is observed to be 0.4 %.

The systematic uncertainty arising from the mass fits is introduced by the chosen fit model and the fixed peaking background yields in the signal channel. Those contributions to the overall uncertainty are estimated by varying the nominal fit model and changing the expected background yield within the uncertainties given by the PIDCalib tool. Fixing only one of the peaking background yields (either $B_s^0 \rightarrow D_s \pi \pi \pi$ or $B_s^0 \rightarrow D_s^* \pi \pi \pi$) and floating the other one during the fit is also considered. The variation in the yield of $B_s^0 \rightarrow D_s \pi \pi \pi$ candidates is found to be negligible ($< 1\%$), when a linear polynomial instead of an exponential is used to model the combinatorial background. Changing the signal component from a double Gaussian model to a Crystal Ball function has no significant effect on the signal yield either. In the signal channel, only a small change of the $N_{B_s^0}$ yield is seen when a single Gaussian signal model is used instead of the nominal double gaussian. The most significant effect is observed when the yield of the $B_s^0 \rightarrow D_s^{(*)} \pi \pi \pi$ misID background is directly determined in the fit. Depending on which component is floated, the signal yield increases or drops by 4%. Since this is the biggest observed effect, we quote it as the uncertainty of the mass fits.

The computed selection efficiency depends on how accurate the momentum spectrum of the final state particles is described by the simulation. To asses a potential systematic uncertainty due to the momentum modeling, we reweight the X_d/X_s mass spectrum in Monte Carlo to agree with our observed signal data. The spectra are shown in Figure 8.1.

Applying the weights, we observe a 0.9 % variation in the selection efficiency of $B_s^0 \rightarrow D_s K \pi \pi$ candidates, while no significant change can be found in the efficiency of the $B_s^0 \rightarrow D_s \pi \pi \pi$ channel.

We use the TISTOS method [8] to cross-check the simulated trigger efficiency on data.

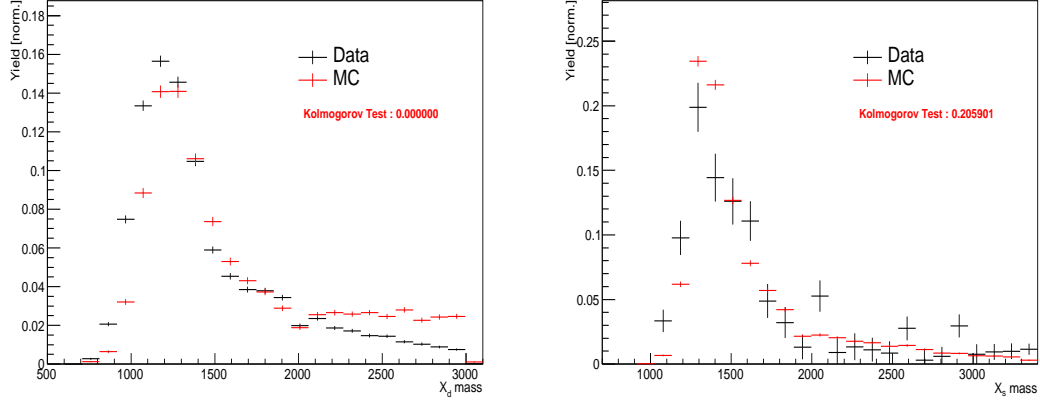


Figure 8.1: Comparison between (left) the X_d invariant mass spectrum and (right) the X_s invariant mass spectrum in (black) data and (red) simulation.

328 The efficiency of the used trigger lines on the signal decay (TOS) is calculated as $\epsilon_{TOS} =$
329 $N_{TIS\&TOS}/N_{TIS}$, where N_{TIS} is the number of signal events which are triggered independent
330 of the signal decay (TIS) and $N_{TIS\&TOS}$ denotes the number of events which are both
331 triggered by signal decays and independently of signal decays. We perform this cross-check
332 using the full sample of $B_s^0 \rightarrow D_s \pi \pi \pi$ decays and the corresponding MC. Figure 8.2 shows
333 the trigger efficiencies for data and MC obtained by the TISTOS method, depending on
334 the highest p_T of the six final state particles, for the L0 and HLT1 trigger stage.

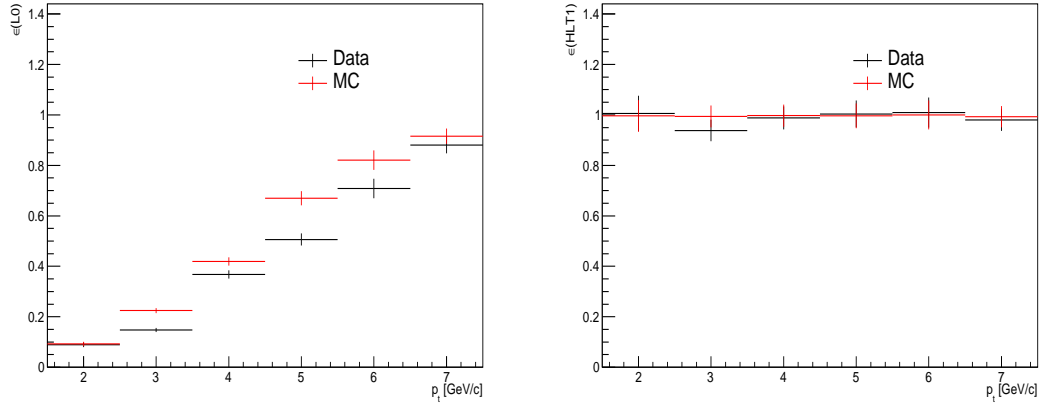


Figure 8.2: Trigger efficiencies of the (lef) L0 and (right) HLT1 trigger stage, determined by the TISTOS method on (black) data and (red) simulation.

335 Although a systematic deviation between the trigger efficiency of the L0 stage in data
336 and MC can be observed, this deviation appears in both the signal and normalization
337 channel and cancels almost completely in every bin of p_T . A small systematic uncertainty
338 of 0.1% remains. The trigger efficiencies for the signal and normalization channel with

respect to the HLT2 stage are compared on MC. An agreement, with deviations being well below the percent level, is observed and thus no systematic uncertainty is assigned to the HLT2 stage.

Due to the different number of hadron types in the final state of the $B_s^0 \rightarrow D_s K \pi \pi$ and $B_s^0 \rightarrow D_s \pi \pi \pi$ decay, a systematic uncertainty related to the tracking efficiency for both channels can arise. To assess a potential difference in the tracking efficiency between the signal and normalization channel, we compare the ratio of the efficiency $\epsilon_{track}(data)/\epsilon_{track}(MC)$ in bins of track momentum p and pseudorapidity η for both MC samples. Figure 8.3 shows the ratio and its p, η dependence for 7 & 8 TeV, using $J/\psi \rightarrow \mu^+ \mu^-$ decays. This table is used to weight the simulated samples according to the pseudorapidity and total momentum of each track.

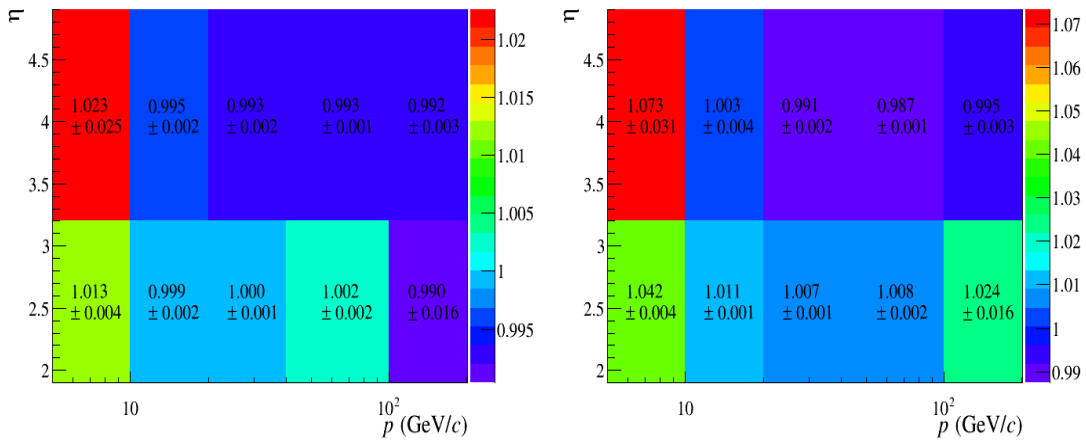


Figure 8.3: Tracking efficiency ratio for data over simulated events for (left) $\sqrt{s} = 7 \text{ TeV}$ and (right) $\sqrt{s} = 8 \text{ TeV}$.

A maximum deviation of $\Delta\epsilon_{track} = 1.5 \%$ can be observed between the signal and normalization channel. Thus, this value is quoted as the systematical uncertainty due to the tracking efficiency.

The uncertainty on the BDTG efficiency is determined by a fit to the $B_s^0 \rightarrow D_s \pi \pi \pi$ invariant mass distribution with and without the BDTG cut. The maximum disagreement is found to be 1.9% and is assigned as the uncertainty on the BDTG efficiency.

The uncertainty due to the limited MC statistic is 1.3% .

All systematic uncertainties are summarized in Table 8.2. The quadratic sum of all contributions is 5.0% .

9 Results and summary

Using the definition of the branching ratio given in Eq. 7.2, we compute from the measured yields and efficiencies:

| Source | Uncertainty on $\frac{\mathcal{B}(B_s^0 \rightarrow D_s K \pi \pi)}{\mathcal{B}(B_s^0 \rightarrow D_s \pi \pi \pi)}$ [%] |
|-----------------------------|--|
| PID | 0.4 % |
| Mass fits | 4.0 % |
| MC efficiency determination | 0.9 % |
| Trigger efficiency | 0.1 % |
| Tracking efficiency | 1.5 % |
| BDTG efficiency | 1.9 % |
| MC statistics | 1.3 % |
| Total | 5.0 % |

Table 8.2: Summary of considered systematic uncertainties on the branching ratio determination.

$$\frac{\mathcal{B}(B_s^0 \rightarrow D_s K \pi \pi)}{\mathcal{B}(B_s^0 \rightarrow D_s \pi \pi \pi)} = 0.051 \pm 0.002 \pm 0.003, \quad (9.1)$$

where the uncertainties are statistical and systematical, respectively.

The results are in good agreement with the first observation and BR measurement of the $B_s^0 \rightarrow D_s K \pi \pi$ decay, done with 1 fb⁻¹ of 2011 LHCb data [4]. The number of signal events already exceeds one thousand candidates, although only the $D_s \rightarrow K K \pi$ final state has been used for this analysis. Adding the $D_s \rightarrow \pi \pi \pi$ final state, which is expected to contribute roughly 20 % of signal on top, makes this channel a promising prospect for a time-dependent γ determination.

A Appendix

A.1 High Level Trigger requirements

The following table summarizes the trigger requirements imposed by the HLT1 line used in this analysis. At least one of the six decay particles must pass the requirements listed in Tab. 1.1 in order for the event to be stored for further analysis.

| Quantity | Hlt1TrackAllL0 requirement |
|------------------------------------|----------------------------|
| Track IP [mm] | > 0.1 |
| Track IP χ^2 | > 16 |
| Track χ^2/nDoF | < 2.5 |
| Track p_T | $> 1.7 \text{ GeV}/c$ |
| Track p | $> 10 \text{ GeV}/c$ |
| Number VELO hits/track | > 9 |
| Number missed VELO hits/track | < 3 |
| Number OT+IT $\times 2$ hits/track | > 16 |

Table 1.1: Summary of the cuts applied by the Hlt1TrackAllL0 trigger. At least one of the six decay particles must pass this requirements, in order for the event to be accepted.

The HLt2 2, 3 and 4-body topological lines use a Boosted Decision Tree based on the b-hadron p_T , its flight distance χ^2 from the nearest PV and the sum of the B_s^0 and D_s vertex χ^2 divided by the sum of their number of degrees of freedom.

A.2 Re-weghted MC observables

Figure ?? shows the distributions of the (left) number of tracks and the (right) maximum ghost probability over all tracks for data, monte carlo and re-weighted monte carlo. These two observables showed significant dissagrement and were therefore chosen for the re-weighting procedure.

The following figures show the comparison of all other observables, which were used during the multivariate selection stage.

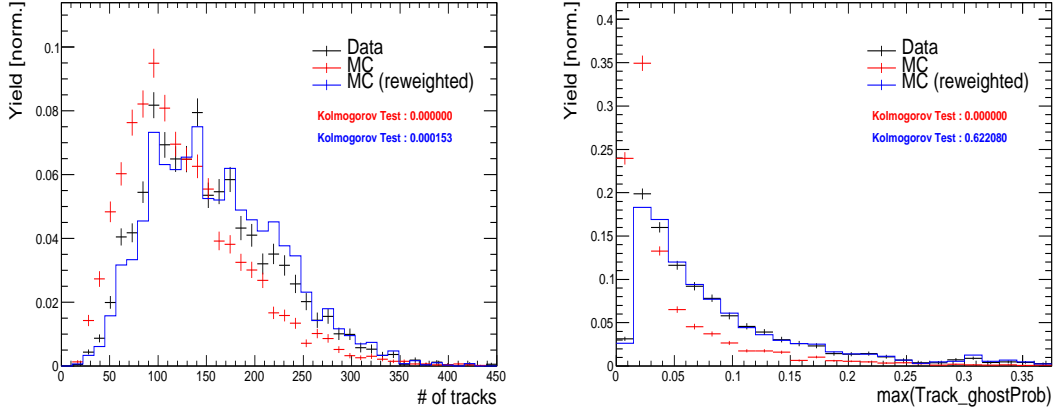


Figure 1.1: Distributions of the (left) number of tracks and the (right) maximum ghost probability over all tracks for data (black), MC (red) and reweighted MC (blue).

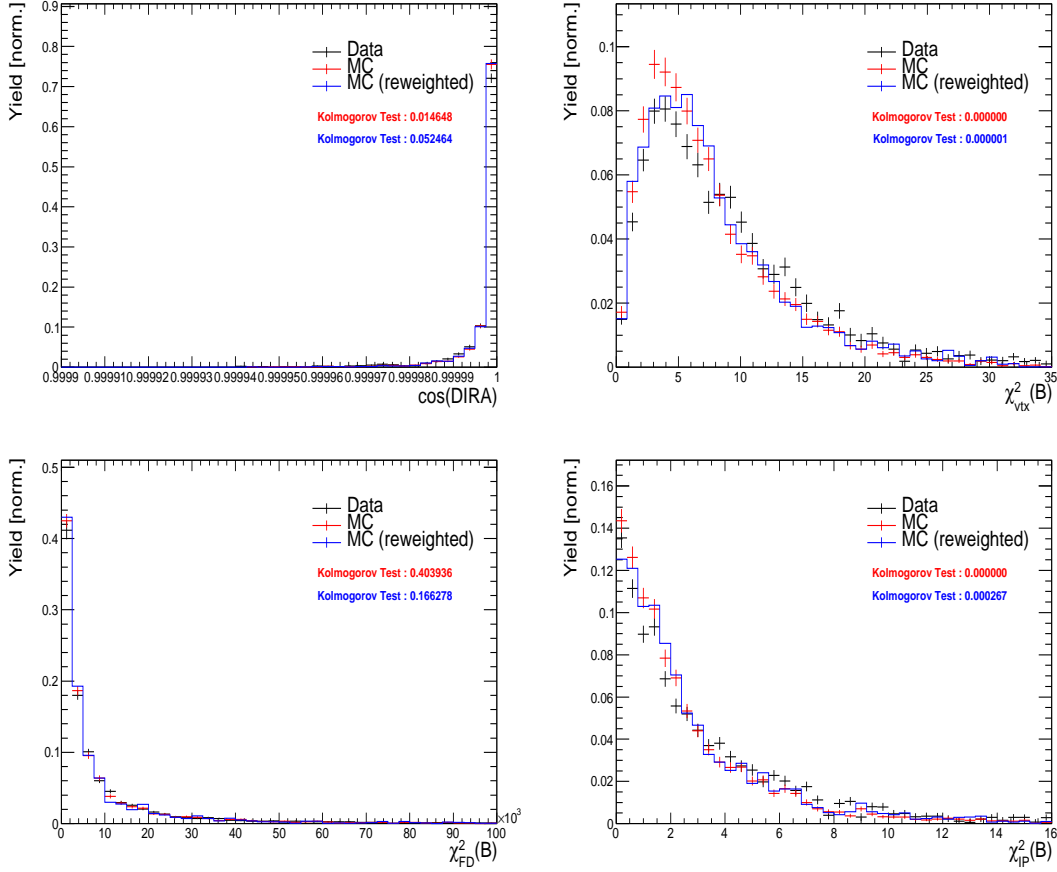


Figure 1.2: Comparison of data and MC observables, before and after reweighting 1.

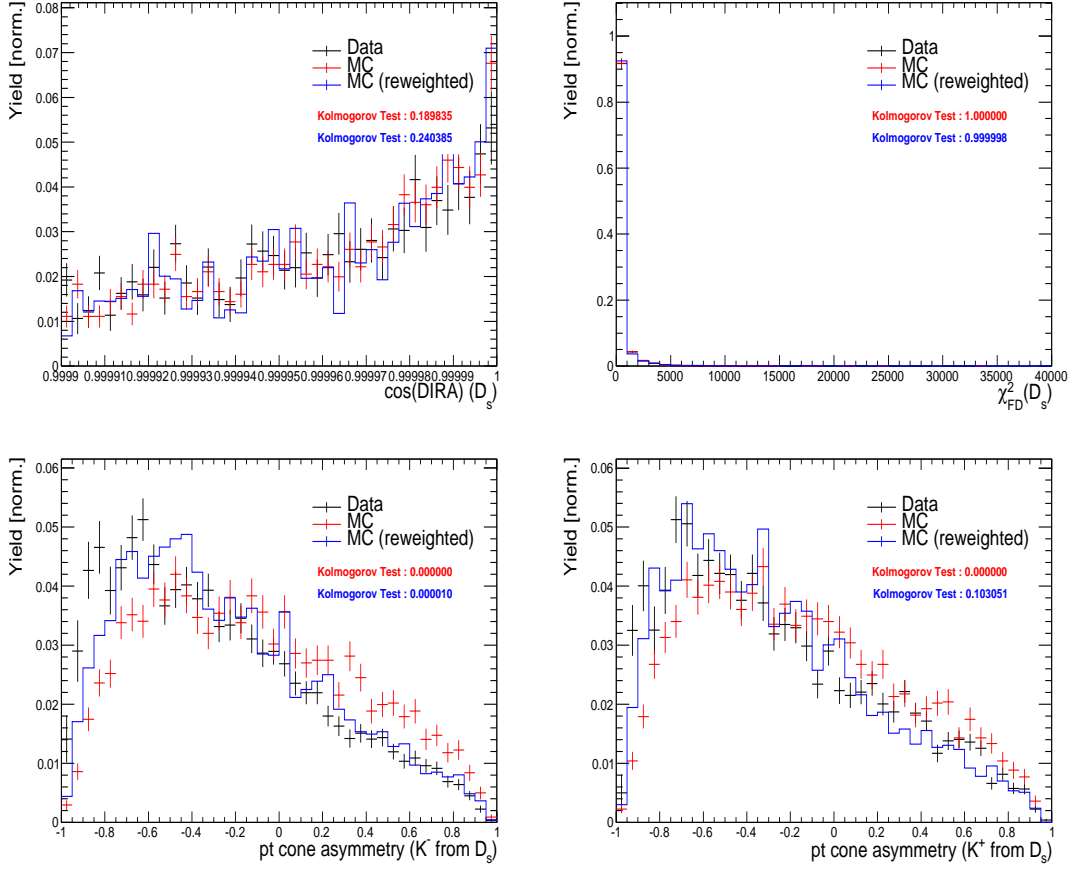


Figure 1.3: Comparison of data and MC observables, before and after reweighting 2.

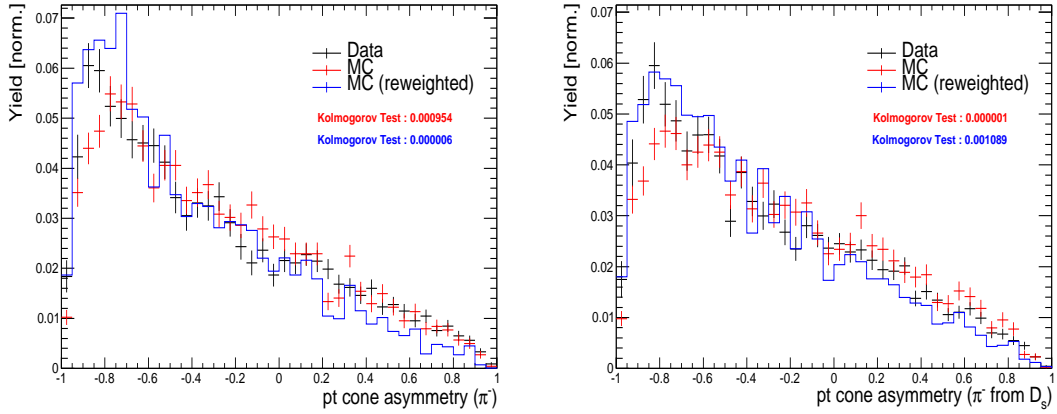


Figure 1.4: Comparison of data and MC observables, before and after reweighting 3.

References

- [1] R. Fleischer, *New strategies to obtain insights into CP violation through $B(s) \rightarrow D(s)^\pm K^\mp$, $D(s)^{\pm*} K^\mp$, ... and $B(d) \rightarrow D^\pm \pi^\mp$, $D^{\pm*} \pi^\mp$, ... decays*, Nucl. Phys. **B671** (2003) 459, [arXiv:hep-ph/0304027](#).
- [2] K. De Bruyn *et al.*, *Exploring $B_s \rightarrow D_s^{(\pm)*} K^\mp$ Decays in the Presence of a Sizable Width Difference $\Delta\Gamma_s$* , Nucl. Phys. **B868** (2013) 351, [arXiv:1208.6463](#).
- [3] S. Blusk, *First observations and measurements of the branching fractions for the decays $\bar{B}_s^0 \rightarrow D_s^+ K^- \pi^+ \pi^-$ and $\bar{B}^0 \rightarrow D_s^+ K^- \pi^+ \pi^-$* , .
- [4] LHCb, S. Blusk, *Measurement of the CP observables in $\bar{B}_s^0 \rightarrow D_s^+ K^-$ and first observation of $\bar{B}_{(s)}^0 \rightarrow D_s^+ K^- \pi^+ \pi^-$ and $\bar{B}_s^0 \rightarrow D_{s1}(2536)^+ \pi^-$* , 2012. [arXiv:1212.4180](#).
- [5] A. Hoecker *et al.*, *TMVA: Toolkit for Multivariate Data Analysis*, PoS **ACAT** (2007) 040, [arXiv:physics/0703039](#).
- [6] M. Pivk and F. R. Le Diberder, *sPlot: A statistical tool to unfold data distributions*, Nucl. Instrum. Meth. **A555** (2005) 356, [arXiv:physics/0402083](#).
- [7] Particle Data Group, K. A. Olive *et al.*, *Review of Particle Physics*, Chin. Phys. **C38** (2014) 090001.
- [8] S. Tolk, J. Albrecht, F. Dettori, and A. Pellegrino, *Data driven trigger efficiency determination at LHCb*, Tech. Rep. LHCb-PUB-2014-039, CERN, Geneva, May, 2014.